

Two Types of Wave Breaking in an Aquaplanet GCM

SUKYOUNG LEE* AND STEVEN FELDSTEIN†

Cooperative Institute for Research in the Environmental Sciences, University of Colorado, Boulder, Colorado

(Manuscript received 9 September 1994, in final form 4 August 1995)

ABSTRACT

The characteristics of two distinct types of wave breaking in an aquaplanet general circulation model (GCM) are described. A systematic analysis of wave breaking is possible because when a baroclinic wave packet is present, the wave breaking tends to occur in the vicinity of the packet center.

Although the refractive index is strictly valid only for linear, quasigeostrophic flows, in this GCM the refractive index is shown to be useful for categorizing two types of wave breaking. Empirical orthogonal function (EOF) analysis is performed using the refractive index obtained (by averaging over one carrier wavelength) at the center of the wave packet. Composite Eliassen–Palm fluxes and upper-level potential vorticity, corresponding to either phase of the first EOF of the refractive index, are consistent with the two types of wave breaking.

It is found that the strength of the meridional shear in the upper troposphere is related to the type of wave breaking. Implications of these results for storm track variability in the atmosphere are also discussed.

1. Introduction

As baroclinic waves lie at the heart of midlatitude atmospheric dynamics, their properties have been studied extensively for many decades. Early theoretical studies of baroclinic waves examined their initial growth with linear stability analysis (e.g., Charney 1947; Eady 1949). Several decades later, after many subsequent investigations that used linear theory, these studies were followed by modeling and observational studies of the full nonlinear growth and decay of baroclinic waves, that is, baroclinic life cycles (e.g., Simmons and Hoskins 1978, 1980; Feldstein and Held 1989; Feldstein 1994; Thorncroft et al. 1993; Randel and Stanford 1985). In so far as the modeling studies are concerned, most of the baroclinic life cycle studies have concentrated on “basic” cases (Simmons and Hoskins 1980) that are characterized by baroclinic growth followed by barotropic decay primarily with largely *poleward* momentum fluxes. An “anomalous” case, which is characterized by largely *equatorward* momentum fluxes, was first described by Simmons and Hoskins (1980) and is given fuller examination in Thorncroft et al. (1993, THM hereafter); in THM, the

anomalous case is characterized as one of two paradigms of baroclinic life cycle evolution, with the other paradigm being the “basic” case. Following THM, we refer to the basic and anomalous cases as LC1 and LC2, respectively.

THM found that the contrast between these two extreme types of life cycles is only apparent during their mature stages, where the nonlinear waves saturate. The mature stage of LC1 was characterized by “anticyclonic” behavior, leading to nonlinear critical-layer absorption equatorward of the westerly jet. On the other hand, the mature stage of LC2 was characterized by “cyclonic” behavior, exhibiting largely undulating potential vorticity contours on the poleward side of the jet, resembling the nonlinear reflection scenario of Rossby wave critical layer theory. Because the life cycles in THM are initiated as a single zonal wavenumber normal-mode instability, the relevance of the linear growth of their life cycle to the atmosphere is questionable. However, THM also showed observational examples of these two distinctly different manners by which the waves break. Throughout this paper, we will refer to these two types of wave breaking as AB (anticyclonic breaking) and CB (cyclonic breaking).

If AB and CB represent two paradigms for wave breaking in the atmosphere, knowledge of AB and CB can also be essential for a better understanding of storm track variability observed in the atmosphere (Blackmon et al. 1977; Nakamura 1992). On the other hand, rudimentary consideration of wave–mean flow interaction tells us that the zonal mean flow changes forced by waves characterized by these two types of wave breaking should be different (e.g., see Fig. 3 in THM). Therefore, the climatology of the midlatitude circula-

* Current affiliation: Department of Meteorology, The Pennsylvania State University, University Park, Pennsylvania.

† Current affiliation: Earth System Science Center, The Pennsylvania State University, University Park, Pennsylvania.

Corresponding author address: Dr. Sukyoung Lee, Department of Meteorology, The Pennsylvania State University, 503 Walker Building, University Park, PA 16802-5013.

tion can crucially depend on the relative importance of AB and CB. The climatology of the zonal mean flow, in turn, is one of the vital elements for low-frequency climate variability; for instance, stationary wave solutions critically depend on the structure of the zonal mean flow (Nigam and Lindzen 1989). Therefore, understanding the behavior of these two types of wave breaking may provide better physical insight into midlatitude atmospheric circulation.

Given these two distinct types of baroclinic wave breaking and their implications for the midlatitude climatology, one wonders if these are indeed two representative paradigms for more realistic situations in the atmosphere; in the life cycle calculations of THM and references therein, a primitive equation model with a single zonal wavenumber (or with higher harmonics) is studied. In a model with a full zonal wavenumber spectrum, where wave-wave interactions take place, it is not immediately obvious how their results will be altered.

However, in trying to answer the question raised above, there are at least two obstacles that are troublesome for an analysis with observational data. First, stationary waves in the atmosphere, which render the basic flow both anticyclonic and cyclonic, may prefer one type of wave breaking over the other at different longitudes (THM). In fact, THM show a case where AB and CB occur at the same time. This may be in part because of the presence of stationary waves. In this case, AB and CB are, to some degree, forced to exist rather than arise from natural variability as a "paradigm" might suggest. Presumably the effect of the stationary wave on the behavior of AB and CB would be smaller in the Southern Hemisphere (SH) due to its smaller stationary wave amplitude, yet it is unclear to what extent their behavior is forced/free in the SH. Second, midlatitude disturbances are typically organized into baroclinic wave packets rather than a uniform wave train consisting of a single zonal wavenumber (Lee and Held 1993; LH hereafter). An exception to this behavior was found by Randel and Stanford (1985), who examined a baroclinic life cycle observed in the Southern Hemisphere (SH), which closely resembles those found in idealized modeling studies with a single zonal wavenumber, for example, Simmons and Hoskins (1978) and Feldstein and Held (1989). However, Randel and Stanford (1985) also stated that this particular case is an exceptionally "clean" example. Clearly, it seems unreasonable to rely on these atypical clean examples for addressing the existence of representative paradigms.

We avoid the first difficulty, namely the existence of stationary waves, by analyzing data from a general circulation model (GCM) with zonally symmetric boundary conditions. An additional advantage of this GCM is that its wave packets are very coherent, and therefore the location of wave breaking can be defined objectively for each model day.

Because the largest wave amplitude occurs near the center of the packet, wave saturation must occur at that location; clearly a linear wave packet can exist due to local excitation of a perturbation, but we believe that the wave packets in the GCM and the atmosphere are by and large nonlinear because of their coherence and persistence. An uncertainty still remains as to how one should categorize AB and CB *objectively*. Because much of the theoretical understanding of nonlinear baroclinic wave evolution has been achieved through zonally symmetric, single-wave lifecycle calculations, we decided to investigate the wave breaking characteristics based on theories of zonally symmetric Rossby wave dynamics. This clearly is a bold assumption, but we are not aware of any theory for zonally asymmetric, nonlinear wave dynamics, based on which one can analyze the occurrence of AB and CB objectively.

Our primary objective in this paper is to address the existence and variability of the two paradigms of Rossby wave breaking in a model atmosphere with a full zonal wavenumber spectrum. This model is described in section 2, together with a full description of our method of analysis. The results are described in sections 3 through 6, followed by concluding remarks in section 7.

2. Model description

a. Aquaplanet GCM

The data from a 2025 day, rhomboidal-30 horizontal resolution, nine vertical level, σ -coordinate, Geophysical Fluid Dynamics Laboratory (GFDL) aqua-planet GCM run are examined. The identical model is also used by LH and Feldstein and Lee (1995). The lower boundary is a flat all-ocean surface with a zonally symmetric sea surface temperature distribution of the form

$$T_s(\phi) = 290 + \left(\frac{40}{3}\right)(1 - 3\sin^2\phi), \quad (1)$$

where ϕ is latitude. The sea surface temperatures are symmetric about the equator and the insolation is specified at the annual mean value. The model uses a full radiation package and hydrologic cycle, including predicted clouds and a moist convective adjustment. Such a model includes the physical parameterizations of a fully realistic GCM, yet it retains the simplicity of a zonally symmetric lower boundary.

b. Making a time series of the "nonlinear wave breaking"

In order to investigate the characteristic behavior of the wave breaking in a systematic manner, as in LH, we first assume that well-defined wave packets exist at each model day and that the region of maximum am-

plitude of the packet can be thought of as the location where the wave breaks. Figure 1 shows a schematic picture of the wave packets. Because the method for determining the location of the packet is fully explained in LH, we will only give a brief description of the procedure here; at each model day, the meridional wind is demodulated so that the location where the maximum amplitude of the packet occurs can be identified. We describe in detail the complex demodulation procedure used in this study in the appendix. Once the carrier wave and the location of the maximum amplitude of the packet is known, we define the "center wave" as the region extending over one carrier wavelength centered at the maximum amplitude of the packet (see Fig. 1).

As we will see later, the difference between the zonal component of the radiative wave activity flux (Plumb 1986) at the two boundaries of the center wave divided by the carrier wavelength is small compared with the wave activity flux divergences in the meridional and vertical directions. Therefore, the conventional EP flux diagnostics can be applied locally. To avoid confusion, we will refer to an average over one carrier wavelength at the center wave (see Fig. 1) as a partial-zonal (PZ, hereafter) average.

3. Examples of AB and CB

Following THM, we use a map of potential temperature, θ , on a constant potential vorticity (PV) surface, defined by $PV = 2$ PVU, where $PVU = 10^{-6} \text{ m}^2 \text{ s}^{-1} \text{ K kg}^{-1}$, to describe atmospheric motion in the upper troposphere. Because the $PV = 2$ PVU surface is a good approximation to the tropopause (Hoskins and Berrisford 1988), a map of θ on that surface gives compact information on the upper-tropospheric PV anomalies. To obtain such a map, we first linearly interpolate the wind and temperature fields from the nine sigma surfaces to nine pressure surfaces. Then, we calculate PV at these nine pressure levels. By additional linear interpolation starting from the uppermost level of the model, we find the value of θ on the 2 PVU surface.

Figures 2 and 3 show two examples of snapshots of θ on the $PV = 2$ PVU surface at five consecutive model days for the AB and CB cases, respectively. We note that the climatological jet, hence the meridional gradient of θ , of this GCM is near 35° . As we will discuss later in this paper, these examples are successfully categorized as the two types of wave breaking using an objective method. In Fig. 2, for the AB case, there is equatorward, wavy, low θ ejection near 30° latitude during all five days. At a given time in this five-day period, there are usually one or two distinct "troughs," with northeast-southwest (NE-SW) tilting, at the center of the packet. This NE-SW tilting is one of the main characteristic features found by THM for the LC1 case. The individual troughs propagate toward the east,

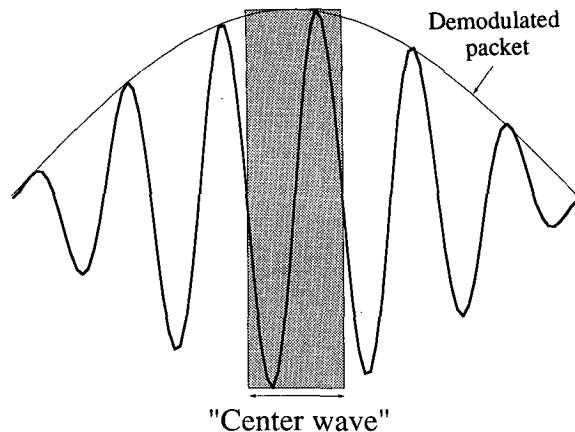


FIG. 1. Schematic diagram of a wave packet. The "center wave" is within the shaded region, and the demodulated packet is also indicated.

but at the same time they grow and decay due to downstream development. Over the five-day period, two troughs undergo such growth and decay. These two troughs are labeled A and B in Fig. 2. At day 1, A is at $\lambda = 130^\circ$, with distinct NE-SW tilting. At day 2, the equatorward tongue of A is substantially thinned as the main part of A propagates about 15° toward the east. By day 3, breaking of the thinning trough A occurs, and another trough to the east of A, trough B, starts to emerge due to downstream development. We also note that there is no clear evidence of NE-SW tilting of B at day 3, but tilting is evident by day 4. At day 5, trough B starts to thin as the NE-SW tilting is progressing. Also, at that time, A is just about to disappear. Eventually, B undergoes decay similar to that for A.

For the CB case (Fig. 3), the structure of θ on the $PV = 2$ PVU surface is quite different from that for the AB case; once again, due to downstream development, there are several troughs that undergo growth and decay at different times, and we refer to these troughs as A, B, and C. At day 1, the cyclone associated with the strong northerly flow at $\lambda = 190^\circ$ starts to intensify at A, and at day 2, as the vortex roll-up progresses, an isolated, cut-off low θ vortex forms in A. At the same time, A moves about 15° toward the east. We also note that the southernmost "edge" of the trough, loosely defined as the region of high θ gradient, appears at least 10° north of that for the AB example. At day 3, while the cutoff low in A is clearly seen at $\lambda = 220^\circ$, trough B at $\lambda = 270^\circ$ starts to develop. By day 4, as A continues to propagate toward the east, it also migrates to the north and decays. At day 5, as another cutoff low starts to form in B, trough C emerges. For the next 5 days or so, similar growth and decay continues.

Unlike for the AB case, these cutoff lows live longer; one still sees the remaining cutoff low from A at day 5. This relative longevity of the cutoff low is consistent

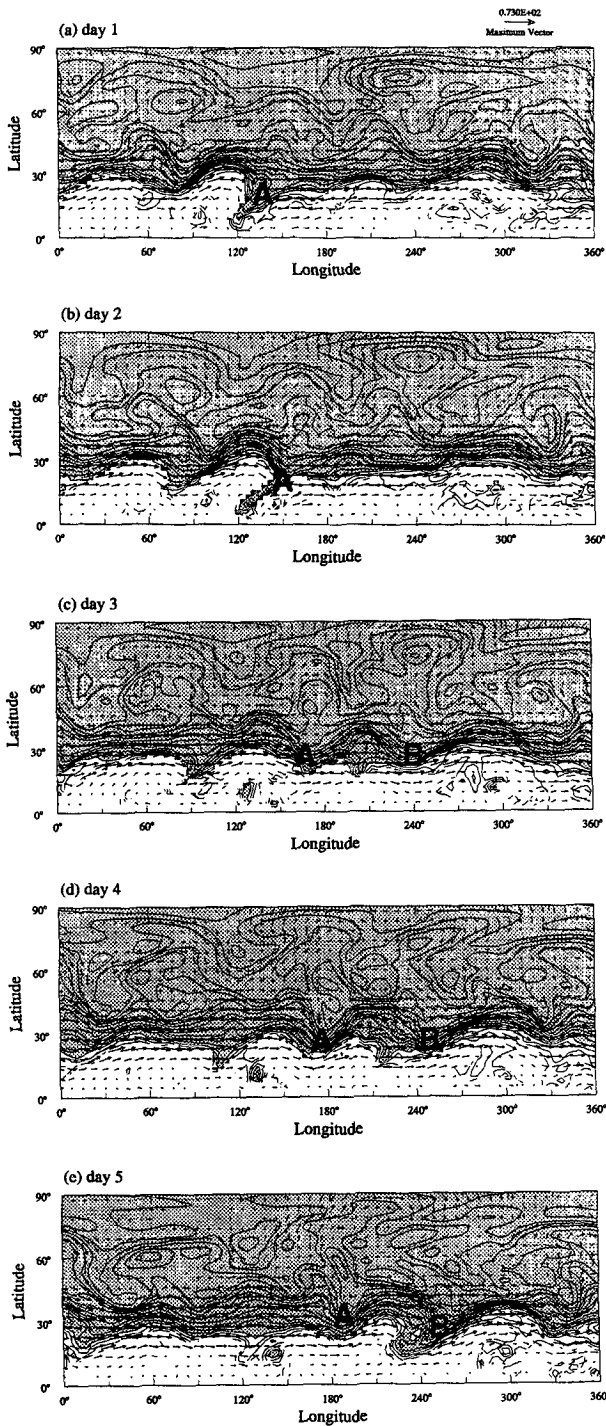


FIG. 2. Snapshots of potential temperature, θ , on the $PV = 2$ PVU surface during (a) day 241–(e) day 245. The contour interval is 5 K, the region where $\theta < 350$ K is shaded, and values of $\theta \geq 365$ K are not plotted.

with the findings of THM. We note, however, that the cutoff low in this GCM decays relatively faster compared to that in the one-wave lifecycle calculation of

THM. In fact, their study finds that the cutoff low “undulates,” showing no sign of decay. We suspect that this difference is at least partially due to the downstream development in the zonal direction in this GCM; for a full zonal wave spectrum, when there is a wave packet, energy can radiate in the zonal direction as well as in the meridional and vertical directions. Clearly, a model with just one unstable zonal wavenumber and its higher harmonics, as in THM, does not have the extra degrees of freedom to radiate energy in the zonal direction.

4. Characterization of wave breaking: EOF analysis

In order to classify the two types of wave breaking in a systematic manner, we investigate the dominant structure of the PZ-averaged (i.e., an average over one carrier wavelength at the center wave) flow. In Simmons and Hoskins (1980) and THM, the basic state for the LC2 case is obtained by adding an appropriate barotropic shear to the LC1 basic state. In other words, a change in the structure of the basic zonal wind was essential for obtaining their two types of lifecycles. The first logical step one should take, then, is to see if there are such zonal wind structures in the GCM that favor either type of wave breaking. For this purpose, we use empirical orthogonal function (EOF) analysis. As we will discuss later, however, the eddy statistics and potential vorticity composites based on the positive (negative) phase of the leading EOF of the quasigeostrophic refractive index obtained from the PZ-averaged fields yields the wave-breaking characteristics of the AB (CB) case, whereas composites based upon the PZ-averaged zonal wind EOFs are not successful. We note that eddy statistics composites shown below do not distinguish AB (CB) from equatorward (poleward) propagation, but each individual case that comprises the composites does show (e.g., see Figs. 2 and 3) such wave breaking.

Although application of the quasigeostrophic (QG) refractive index (Matsuno 1970; Karoly and Hoskins 1982; Palmer 1982) is strictly valid only for linear wave dynamics, as shown in Randel (1985) for observations and in Feldstein (1994) and THM for nonlinear life cycle calculations, the QG refractive index appears to be quite a useful tool for understanding wave-propagation characteristics. For this reason, and for the reason that the PZ-averaged zonal wind EOFs are found to be rather unsuccessful in distinguishing the AB and CB cases, we first examine EOFs of the QG refractive index. In some sense, the QG refractive index is actually expected to be a better quantity for characterizing AB and CB than the PZ-averaged zonal wind, U , since the QG refractive index, which is dependent upon U among other quantities, is more closely tied to wave propagation, at least in a linear context. The QG refractive index on a sphere is given as

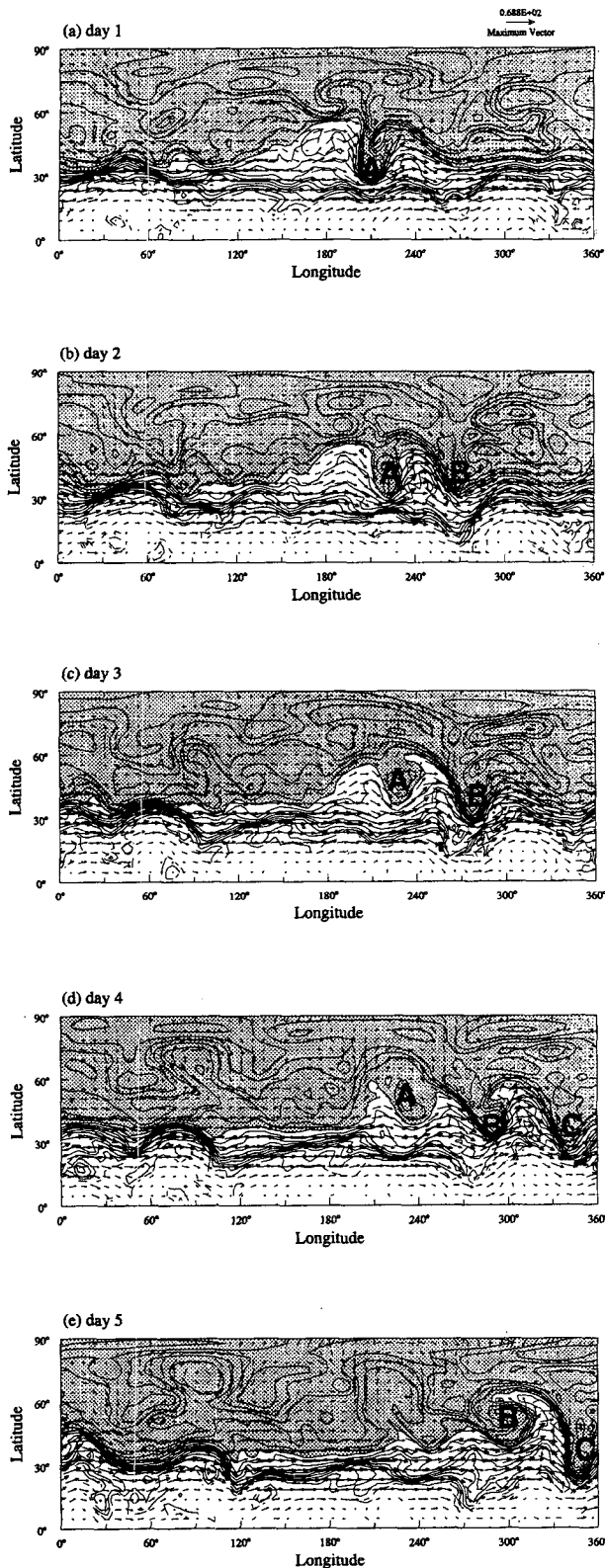


FIG. 3. Snapshots of potential temperature, θ , on the $PV = 2$ PVU surface during (a) day 154–(e) day 158. The contour interval is 5 K, the region where $\theta < 320$ K is shaded, and values of $\theta \geq 0.365$ K are not plotted.

$$n^2 = \left[\frac{\partial Q / \partial y}{U - ca \cos \phi} - \frac{f^2}{4H^2 N^2} - \frac{k^2}{a^2 \cos^2 \phi} \right] / (\sin^2 \phi), \quad (2)$$

where c is the angular velocity of the disturbance, a the earth's radius, N the Brunt-Väisälä frequency, H the scale height, f the Coriolis parameter, and k the zonal wavenumber. The quasigeostrophic meridional potential vorticity gradient, $\partial Q / \partial y$, is

$$\frac{\partial Q}{\partial y} = \frac{2\Omega \cos \phi}{a} + \frac{1}{a} \frac{\partial \zeta}{\partial \phi} - f^2 \frac{\partial}{\partial p} \left[\left(\frac{\rho g}{N} \right)^2 \frac{\partial U}{\partial p} \right], \quad (3)$$

where ζ is the PZ-averaged relative vorticity, U the PZ-averaged zonal wind, ρ the density, g the gravitational acceleration, and p the pressure. The basic properties of n^2 are that regions of positive (negative) refractive index are characterized by propagation (evanescence). In regions of propagation, Eliassen-Palm (EP) flux vectors are refracted toward larger n^2 . Furthermore, points where $U - ca \cos \phi$ equals zero, that is, an infinite refractive index, correspond to a critical surface, and points where n^2 equals zero indicate the location of a turning surface. According to linear quasigeostrophic theory, for plane-parallel shear flows with positive $\partial Q / \partial y$ everywhere, disturbances are absorbed (reflected) at critical (turning) surfaces. In order to compute the refractive index, we use the PZ-averaged zonal wind and temperature and also fix the values of k and c at 6 and $2.0 \times 10^{-6} \text{ s}^{-1}$, respectively. The values of k and c were estimated 1) from a power spectrum of the eddy streamfunction as a function of both zonal wavenumber and frequency, and 2) from a one-point correlation map of the eddy streamfunction (see LH). Both methods give consistent estimates. We also calculated the refractive index using other values of k and c , that is, $5 \leq k \leq 7$, and $1.6 \times 10^{-6} \text{ s}^{-1} \leq c \leq 2.4 \times 10^{-6} \text{ s}^{-1}$. There are slight changes in the location of the critical and turning latitudes, but the important qualitative features of the time-mean n^2 as well as the first and second EOFs of n^2 , $e_1(n)$ and $e_2(n)$, respectively, are found to be insensitive to these changes. We also note that because a very large variance in the EOF analysis can occur when a grid point is very close to a critical latitude, we set the value n^2 at a maximum value of $4 \times 10^{-13} \text{ m}^{-2}$. The sensitivity of our EOF analysis to this maximum value, varied over a wide range of settings, was found to be small.

The time-mean n^2 from the region of the center wave is shown in Fig. 4a. Due to the time-averaging, the contours are not greatly packed together on the equatorward side of the propagation region, where the critical latitude is present. In the upper troposphere, poleward of the jet, zero values for n^2 indicate both a turning level and turning latitude.

The structure of $e_1(n)$ is illustrated in Fig. 4b. We found that the variances of the first two EOFs are 14.9% and 11.7%, respectively, and that they are distinct

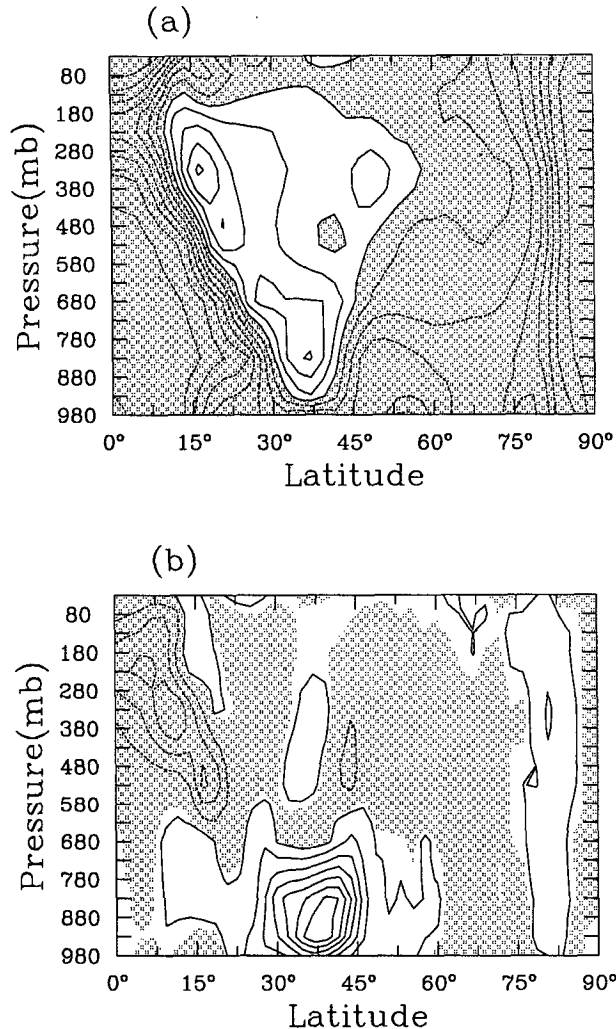


FIG. 4. Meridional cross section of the (a) time-mean quasigeostrophic (QG) refractive index and (b) the first EOF of the QG refractive index. The contour interval for (a) is $5 \times 10^{-14} \text{ m}^{-1}$, and the contour interval for (b) is arbitrary. In both (a) and (b), the negative region is shaded.

(North et al. 1982). The main features of $e_1(n)$, by adding and subtracting this EOF to the time-mean n^2 , are 1) an extension (contraction) of the propagation region in the upper troposphere for the negative (positive) phase and 2) an equatorward (poleward) shift of the critical latitude on the equatorward side of the jet for the negative (positive) phase. The second EOF (not shown) mainly represents latitudinal shifts of the propagation region throughout the entire region of the climatological zonal jet.

The EP flux vector, which is closely related with the QG refractive index, has been found by THM to be useful for describing the characteristics of wave-activity propagation for the nonlinear evolution of their two types of lifecycles that illustrate AB and CB (see also

Edmon et al. 1980). Therefore, we examine the EP flux vectors and their divergence to see if the wave propagation characteristics associated with the leading refractive index EOF are consistent with those for the mature stage of the LC1 and LC2 cases of THM, and therefore for the AB and CB cases. We use the primitive equation form of the EP flux vector (Andrews and McIntyre 1976) in pressure coordinates and write the EP flux vector as $\mathbf{F} = (0, F^{(\theta)}, F^{(p)})$, where

$$F^{(\theta)} = a \cos \phi \left(-\overline{u'v'} + \frac{\overline{v'\theta'}}{\partial\theta/\partial p} \frac{\partial U/\partial p} \right) \quad (4.a)$$

$$F^{(p)} = a \cos \phi \left(f_a \frac{\overline{v'\theta'}}{\partial\theta/\partial p} - \overline{u'w'} \right), \quad (4.b)$$

where (u, v, w) are the velocities in pressure coordinates, θ the potential temperature, and f_a the absolute vorticity. The overbar denotes a PZ-average and the prime a deviation from the PZ-average. The EP fluxes associated with $e_1(n)$ are obtained by compositing \mathbf{F} based on either phase of $e_1(n)$. There are three conditions that we require for the composites: 1) the value of the principal component of the EOF should be within the top (most positive) or bottom (most negative) 10%. For the entire 2025 day time series, a total of 202 cases qualified for each phase. In order to ensure that the wave packet is well defined at a given time, we require that 2) the half-width of the demodulated envelope be smaller than 180° longitude. If there is a second peak in the envelope, it should be smaller than the amplitude of the envelope at the half-width. This condition usually eliminates one-third of the candidates that satisfy the first criterion. Lastly, 3) we require that the dominant zonal wavenumber be either 5, 6, or 7, in order to make sure that the wavenumber of the center wave remains close to 6, which is consistent with the above refractive index calculation. Also, the zonal wavenumber power spectrum peaks at wavenumber 6. About 90% of the candidates that satisfy both 1) and 2) fall into this criterion. We also have examined the full zonal mean quantities and found that the differences in eddy statistics and zonal winds between the AB and CB cases are very small, indicating that the distinction of the flow characteristics that will be described below is zonally confined. If the same composites are performed over two wavelengths about the center of the packet, the same basic composite pattern is found as with the single wavelength average, but with a smaller amplitude.

Figures 5a and 5b shows the composite EP fluxes based on the positive and negative phases of the first refractive index EOF, respectively. There are 117 and 113 samples for the positive and negative phases, respectively. For the positive phase, as in the LC1 case of THM, there is an EP flux divergence-convergence pair in the upper troposphere, with the convergence on the equatorward side of the jet coinciding with equatorward-pointing horizontal vectors. Also, there is a

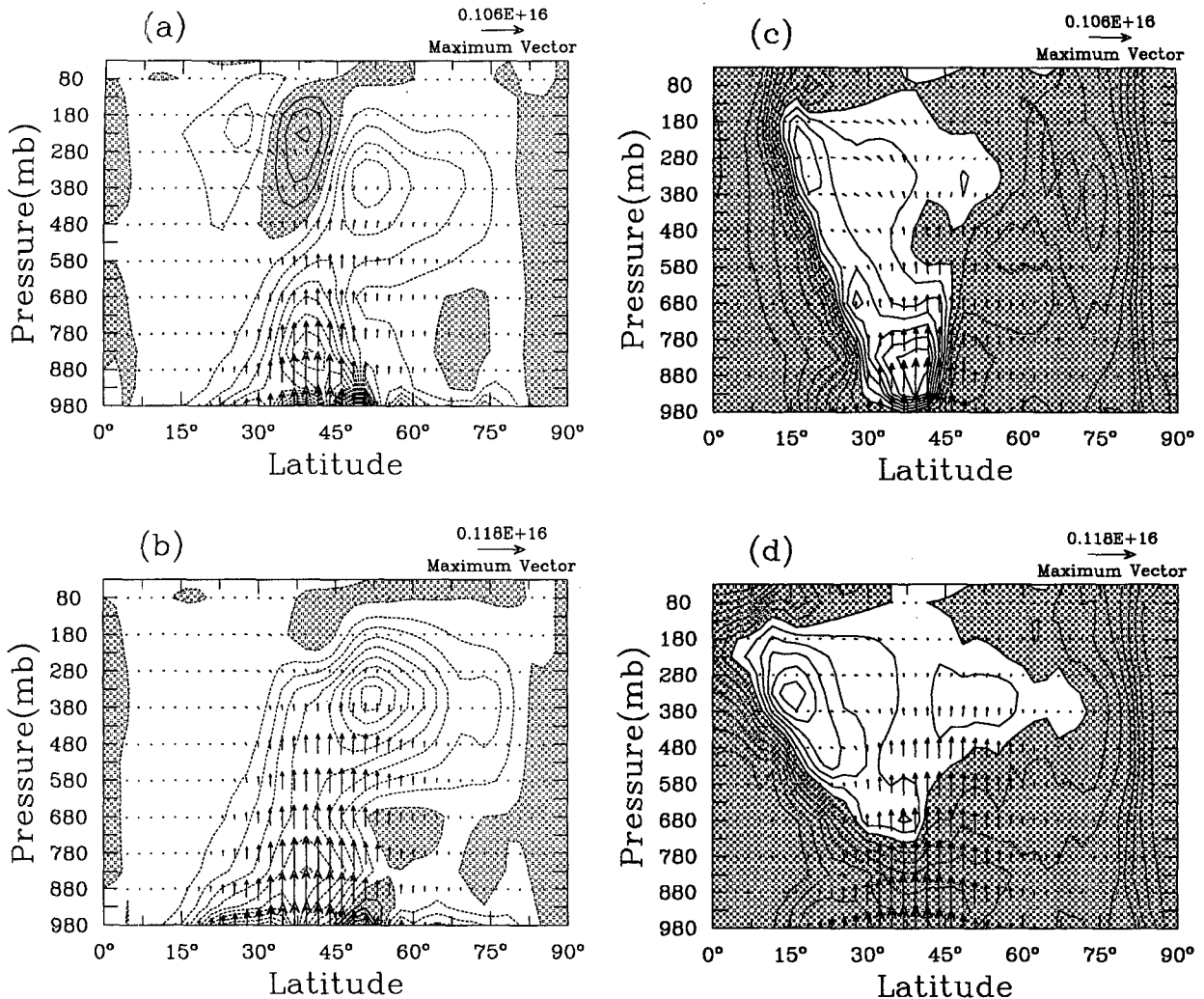


FIG. 5. Meridional cross section of the positive phase composite (a) EP flux and its divergence, (c) QG refractive index, (e) eddy kinetic energy, and (g) PZ-averaged zonal wind for $e_1(n)$. Meridional cross section of the negative phase composite (b) EP flux and its divergence, (d) QG refractive index, (f) eddy kinetic energy, and (h) PZ-averaged zonal wind for $e_1(n)$. The difference between (e) and (f) is shown in (i), and the difference between (g) and (h) is shown in (j). The contour interval for (a) and (b) is $3 \times 10^{-5} \text{ m s}^{-2}$, (c) and (d) is $5 \times 10^{-14} \text{ m}^{-1}$, (e) and (f) is $20 \text{ m}^2 \text{ s}^{-2}$, (g) and (h) is 5 m s^{-1} , (i) is $10 \text{ m}^2 \text{ s}^{-2}$, and (j) is 1 m s^{-1} . In (a), (b), (i), and (j), regions with positive values are shaded. In (c) and (d), regions with negative values are shaded. In (e) and (f), the region where $\text{EKE} > 200 \text{ m}^2 \text{ s}^{-2}$, and in (g) and (h), the region where $U > 30 \text{ m s}^{-1}$ are all shaded.

broad region of EP flux convergence throughout the lower troposphere. However, unlike the LC1 case of THM, there is also a region of EP flux convergence on the poleward side of the jet in the middle to upper troposphere. This poleward convergent region is twice as strong as that on the equatorward wide of the jet. This convergence is mainly due to vertical pointing vectors, that is, due to the meridional heat flux. We suspect that this convergence stems from the equatorward positioning of the climatological jet in this GCM; the third term on the right-hand side of (3) indicates that a smaller f favors a positive refractive index. As the jet is equatorward of that in

THM, the poleward side of the jet is also closer to the equator, where f is smaller. Therefore, wave activity can more easily propagate toward the poleward side of the jet. For the negative case (Fig. 5b), the EP flux vectors point mostly upward and are located primarily on the poleward side of the jet, as in the LC2 case of THM. On the equatorward side of the jet, there are equatorward-pointing vectors with small amplitude, as in the LC2 case of THM (see their Fig. 15f). Also, except near the regions where the value of the EP flux divergence is close to zero, the main structures shown in Figs. 5a and 5b are statistically significant above the 95% level.

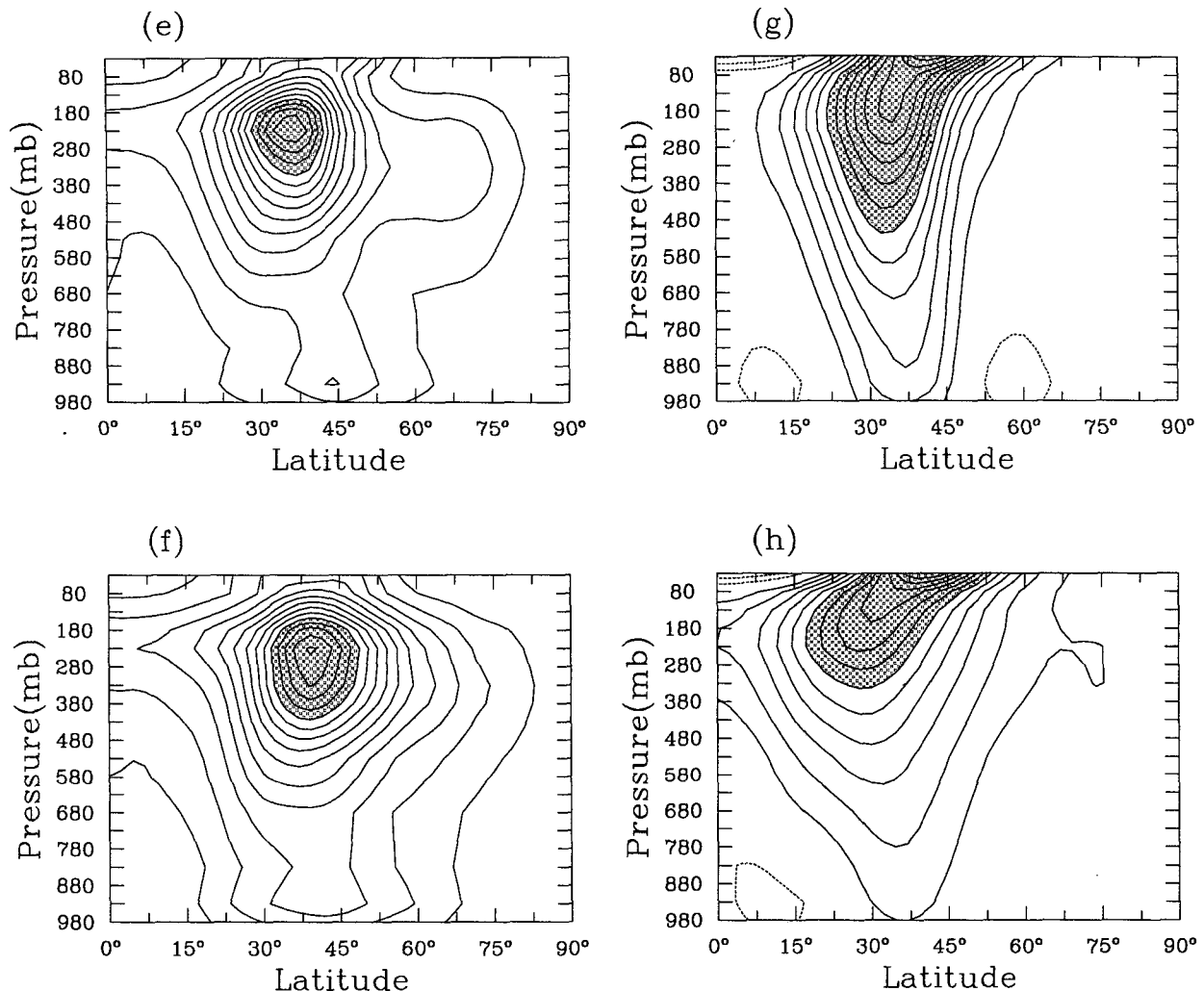


FIG. 5. (Continued)

The next obvious question is whether or not the foregoing description of the EP fluxes are consistent with the properties of the QG refractive index. Figures 5c and 5d show the composite QG refractive index, n^2 , for the positive and negative cases, respectively, upon which the corresponding composite EP flux vectors are superimposed. By definition, one can also think of these composite n^2 as the superposition of the time-mean n^2 and either phase of $e_1(n)$ shown in Fig. 4. Although not a perfect match, one can see many properties of the composite EP flux vectors that are indeed consistent with theory. For example, in both cases shown in Fig. 5, the composite EP flux vectors in the middle and upper troposphere are mostly confined to within the positive n^2 region. The region of large amplitude EP flux vectors in the negative n^2 region of the lower troposphere may at first appear to be inconsistent with linear theory. However, as described in the baroclinic lifecycle study of Feldstein (1994), such behav-

ior is required for linearly unstable flows according to the theory of critical-level overreflection [for a summary of critical-level overreflection and its relationship to linear instability, see Lindzen (1988)] for plane-parallel shear flows. Furthermore, in the positive n^2 region for both phases, one can see the tendency for the EP flux vectors to be refracted toward larger n^2 . One can also see interesting differences in the EP flux diagrams for the two phases of $e_1(n)$. For example, the EP flux vectors for the positive phase are confined to a narrower range of latitudes and exhibit stronger equatorward propagation when compared to the negative phase. These characteristics are also consistent with theory.

One of the main characteristics of the two baroclinic waves in THM is that the eddy kinetic energy (EKE) attains a larger amplitude for the LC2 case. Because the maximum EKE is primarily determined by the manner through which the wave saturates, and not by the linear growth rate, we expect that our CB case will also

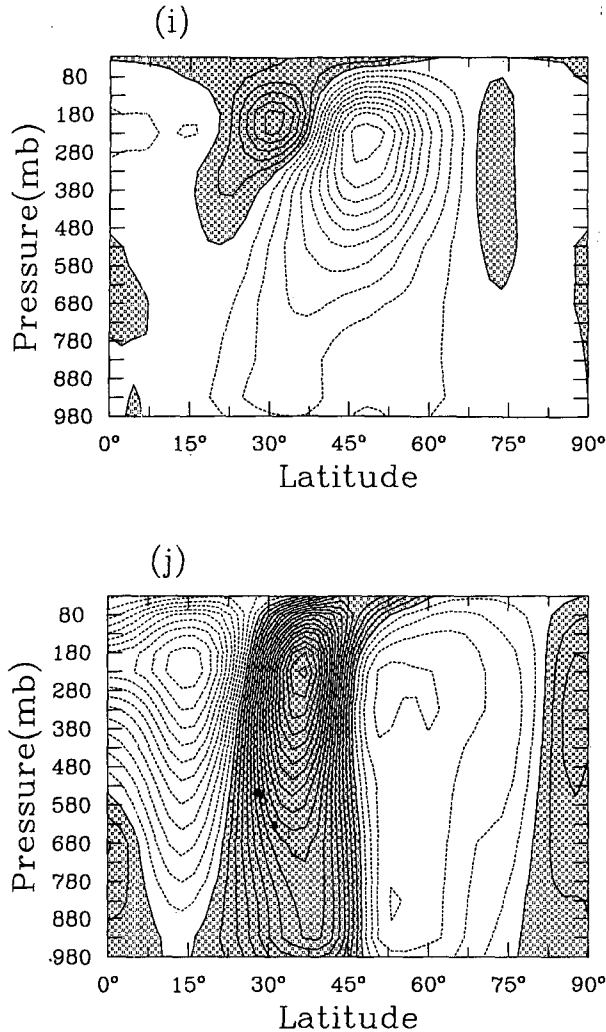


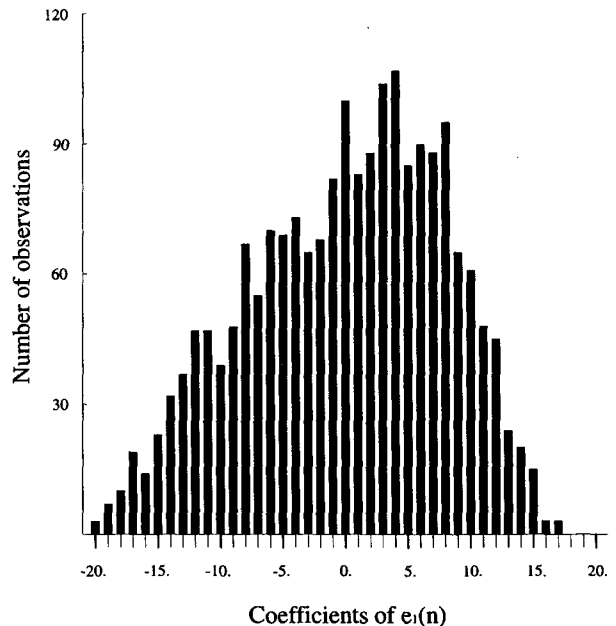
FIG. 5. (Continued)

attain larger EKE than the AB case. Figures 5e and 5f show the composite EKE for the positive and negative cases, respectively. The region where EKE values exceed $200 \text{ m}^2 \text{ s}^{-2}$ is shaded. In both cases, the largest EKE amplitude is in the upper troposphere. Once again, consistent with THM, the maximum EKE is somewhat greater for the negative than for the positive phase. Also, the location of the maximum EKE for the negative phase is about 5° poleward of that for the positive phase. These differences are apparent in Fig. 5i, in which the EKE for the negative phase is subtracted from that of the positive phase.

The composite PZ-averaged zonal winds for the positive and negative phases of $e_1(n)$ are shown in Figs. 5g and 5h, respectively. It is clear that the zonal jet for the negative case is wider than that for the positive case. At the same time, the maximum amplitude of the jet is smaller for the negative case than that for the positive case. Also, the jet core tilts more strongly equatorward

with increasing height for the negative case. The difference in the composite PZ-averaged zonal wind, the negative case subtracted from the positive case, is shown in Fig. 5j. The essential difference between these two cases is the equivalent barotropic shear with two nodes, one equatorward and the other poleward of the climatological jet (see Fig. 12a); cyclonic (anticyclonic) shear is stronger on the equatorward (poleward) side of the jet for the negative phase when compared to the positive phase. Also, for the negative phase, the cyclonic shear on the equatorward side of the jet is stronger than the anticyclonic shear on the poleward side of the jet. In any case, the difference between the zonal wind for the positive and negative cases is somewhat more complex than that between the LC1 and LC2 cases in THM. We also note that the equatorward node, near 25° latitude, is very close to the jet core in the upper troposphere. In light of the basic states of THM, namely that the basic state for the LC2 case is obtained by adding cyclonic, barotropic shear to the basic case for the LC1 case, the above analysis suggests that it is the cyclonic shear in the upper troposphere that accompanies CB.

We conclude this section by noting that a histogram of the principal component of $e_1(n)$ is skewed toward the positive phase (see Fig. 6). The maximum frequency occurs between values of 4.5 and 6.5 for the principal component. A similar analysis was performed separately for the first and second 1000 days of the model integration. Both analyses revealed skewed histograms that closely resembled that shown in Fig. 6. Because of the relationship between the PZ-averaged

FIG. 6. Histogram of the principal component (coefficient) of $e_1(n)$.

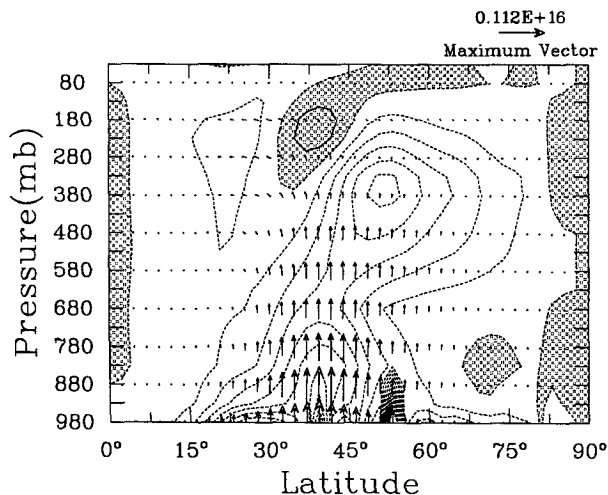


FIG. 7. Time-mean EP cross section for the center wave. The contour interval is $3 \times 10^{-5} \text{ m s}^{-2}$, and regions with positive EP flux divergence are shaded.

flow and the type of wave breaking, a possible interpretation of the asymmetric structure in the histograms is that AB is more typical in this model. Perhaps this is to be expected for at least two reasons: the metric terms that arise from the earth's sphericity favor anticyclonic over cyclonic wave development (Whitaker and Snyder 1993), and typically the critical latitudes on the equatorward (poleward) side of the jet are closer to (farther from) the midlatitude disturbances, causing a latitudinal asymmetry in the baroclinic waves; Nakamura and Plumb (1994) examined the direction of wave breaking in a shallow water model using contour dynamics and found that waves break toward the side of the jet where the critical latitude is closer. However, it should be borne in mind that the variance of $e_1(n)$ is only 14.9%, and therefore one needs to be careful when interpreting the histogram described above. Therefore, we feel that it is also important to discuss the structure of the time-mean baroclinic waves. For this purpose, we examine the composite EP cross section with the first of the three composite conditions relaxed but with the second and third conditions retained (see Fig. 7). There are 1178 cases that satisfy the latter two conditions. The resulting composite EP fluxes show characteristics that are intermediate between those of the positive and negative cases; the equatorward-pointing vectors and the divergence region in the upper troposphere are smaller than those of the positive case (Fig. 5a) but greater than those of the negative case (Fig. 5b); the poleward- and upward-pointing vectors and the poleward convergence in the upper troposphere are greater than those of the positive case, but smaller than those of the negative case. Given the greater wave amplitude for the negative case (CB), even if there is a higher probability for the positive case (AB) to occur

in this GCM, it may not be surprising that the time-mean waves show characteristics between those of the two cases.

5. Horizontal structure of the wave packets

In the foregoing analysis, we showed that the eddy statistics and local background flow composites based on the positive (negative) phase of $e_1(n)$ are consistent with the wave saturation stage of LC1 (LC2) of THM, and therefore it was implied that AB and CB can be objectively distinguished based on zonally symmetric, linear wave theory. However, the underlying dynamics behind the zonally localized wave packet adds great complexity to the zonally averaged, two-dimensional view of the single zonal wavenumber dynamics. We do not attempt to solve this additional complex problem here, but we describe the rudimentary three-dimensional structure of the wave packets for both the posi-

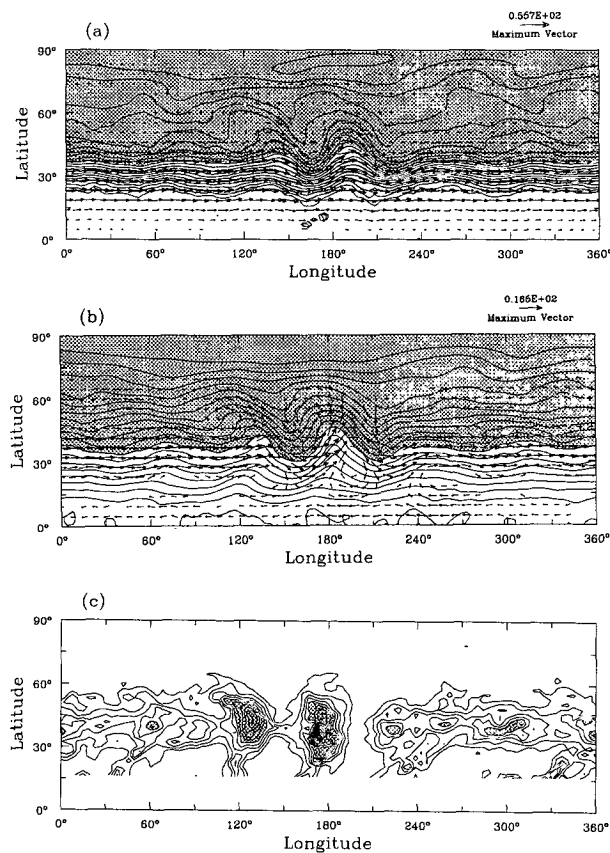


FIG. 8. Composite (a) θ on the $PV = 2 \text{ PVU}$ surface, (b) θ on the 830-mb surface, and (c) precipitation rate for the positive phase of $e_1(n)$. For the cases selected, the dominant zonal wavenumber is 6. The contour intervals are (a) 3 K, (b) 2 K, and (c) 0.1 cm day^{-1} . Regions where (a) $\theta < 320 \text{ K}$, (b) $\theta < 290 \text{ K}$, and (c) greater than 0.6 cm day^{-1} are shaded. In (c), contours values of zero and 0.1 are omitted for clarification.

tive and negative phases to give readers a better picture of the wave packet structure.

For the composite maps presented in Figs. 8 and 9, in order for the individual wave structure to be preserved, the entire field is phase-shifted so that the local maximum in the 205-mb meridional wind near the packet center lies at a common longitude of 180° . Also, we add one extra condition to the composite; we only include those cases where the dominant zonal wavenumber is 6. Composites where the dominant zonal wavenumber is 5 or 7 remain qualitatively very similar.

Figures 8a and 9a show the composite potential temperature, θ , on the PV = 2 PVU surface for the positive and negative phase of $e_1(n)$, respectively. Compared with the snapshots of θ on the PV = 2 PVU surface (see Figs. 2 and 3), the wave structure is smoother due to the compositing procedure. However, one sees NE–SW tilt for the positive (Fig. 8a) and NW–SE tilt for the negative (Fig. 9a) cases. We recall that these tilts are noted as one of the main characteristics for AB and CB in section 3. Therefore, although it is impossible to see AB on the equatorward side of the jet in Fig. 8a and CB on the poleward side of the jet in Fig. 9a, they are clearly consistent with the results found in section 3.

Thinking of the atmosphere as analogous to the Eady model, we regard θ on the PV = 2 PVU surface as the potential vorticity on the upper boundary. Similarly, the potential temperature at lower levels in this GCM may be referred to as the potential vorticity on the lower boundary. We regard the 830-mb level as the lower boundary for this purpose because the model levels below 830 mb in this all ocean GCM are rather strongly affected by the boundary-layer mixing parameterization. Figures 8b and 9b show θ on the 830-mb surface for the positive and negative phases, respectively. For convenience, we call the θ on the PV = 2 PVU and 830-mb surfaces “upper PV” and “lower PV,” respectively. For both the positive and the negative phases, the upper-level horizontal winds are in general parallel to the contours of upper PV, but the lower-level winds have a strong component crossing the lower PV contours; to the east of the packet center ($\lambda > 180^\circ$), the upper- and lower-level winds are almost in phase, while the PV anomalies, that is, the “ridges” and “troughs,” are not. This results in new trough development at the lower level near $\lambda = 210^\circ$, downstream of the packet center, because of advection of the θ contours. This downstream development is more clearly visible for the negative case (Fig. 9b). Because the lower-level winds downstream of the packet center are almost parallel to the upper PV contours, we believe that the lower-level winds are associated with the upper PV anomaly and that these winds induce the lower PV anomaly downstream of the packet center (see Hoskins et al. 1985). This is consistent with the local energetic analysis of Orlanski and Chang (1993) and Chang (1993), where they show that the downstream ageo-

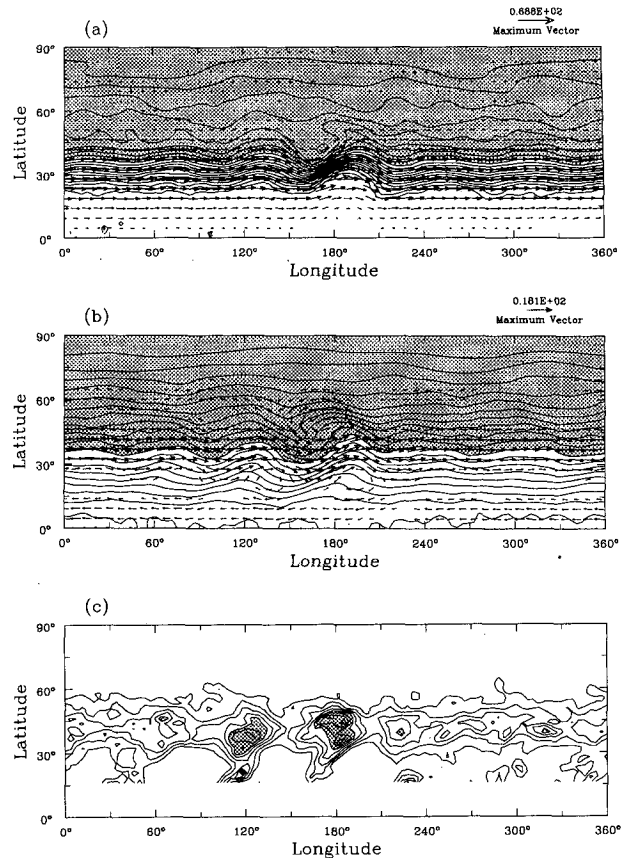


FIG. 9. The same as Fig. 8 except for the negative phase of $e_1(n)$.

strophic fluxes lead baroclinic growth. In principle, PV inversion can either confirm or refute this speculation.

Figures 8c and 9c show the precipitation rate for the positive and negative cases, respectively. To focus on midlatitudes, the precipitation rate equatorward of 15° latitude is not shown. We first note that the precipitation rate for both cases is remarkably well organized, as the wave packet structure itself, and second that the maximum precipitation rate for the negative case is more than twice that for the positive case.

We complement the above description with the radiative wave activity flux vector, defined by \mathbf{M}_R , in Plumb (1986). As there is no stationary wave in our model, we can think of the basic flow as “pseudo-eastward” (see Plumb 1986). Therefore, we use a simpler form of \mathbf{M}_R :

$$\mathbf{M}_R = \frac{p}{p_0} \cos \phi \left[(\overline{v'^2} - \epsilon), -\overline{u'v'}, \frac{f/\rho g}{d\theta/dp} \overline{v'\theta'} \right], \quad (5)$$

where p is the pressure, p_0 the mean surface pressure, and ϵ the wave energy density defined in (2.12) of Plumb (1986). Other notations are standard. Figures 10a and 10b show zonal cross sections of the \mathbf{M}_R vector at 35° latitude for the positive and negative cases, re-

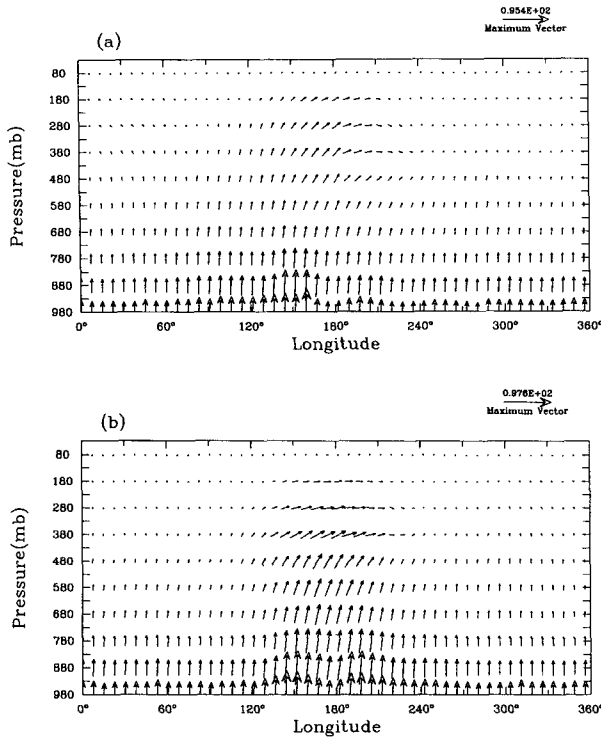


FIG. 10. Zonal cross section of the M_R vector, defined by (5), at 35° latitude for the (a) positive and (b) negative phases of $e_1(n)$.

spectively. For both cases, in the lower (upper) troposphere the vertical (horizontal) component of M_R dominates and is primarily upward (eastward). The positive zonal component of M_R , indicating an eastward group velocity relative to the time-mean flow, is consistent with downstream development confined to the upper troposphere, as discussed previously in this paper. Noting that the meridional and vertical components of M_R [see (5)] are identical with those of the QG version of the EP flux vector for a zonally symmetric flow, it is clear that (5) is a three-dimensional, QG generalization of (4), as Plumb (1986) pointed out. Because the values of the zonal component of M_R at either boundary of the center wave (refer to Fig. 1) are similar, as shown in both Figs. 10a and 10b, it is not surprising that the diagnostics based on a zonally symmetric flow in section 4 turned out to be useful. In both cases, the horizontal cross section of M_R (see Fig. 11) in the upper troposphere indicates vectors directed away from the jet center at the center wave. The vectors on the equatorward side of the jet dominate for the positive phase, whereas the vectors on either side of the jet are approximately of equal magnitude for the negative phase. This behavior is consistent with the composite potential temperature maps shown in Figs. 8a and 9a.

The above results with the M_R vector suggest the following qualitative description for the disturbance

evolution within the wave packet. First, we recall that for both the positive and negative cases (Figs. 10a and 10b), the M_R vector in the upper troposphere has a large zonal component. The zonal component of M_R is divergent (convergent) upstream (downstream) of the packet center, which indicates a decrease (increase) of wave activity upstream (downstream) of the packet center. Such behavior is representative of an eastward-propagating packet that is undergoing downstream development. Furthermore, the M_R vectors have a large vertical (meridional) component at the packet center in the lower (upper) troposphere, indicating baroclinic growth (barotropic decay). Also, since it was previously shown that disturbances within the upper troposphere appear to precede those in the lower troposphere, this baroclinic growth is most likely due to ‘‘Petterssen Type B cyclogenesis’’ (Petterssen 1956).

From a global energetics viewpoint, the above zonal dispersion of wave activity plays no role, but the baroclinic growth at the packet center is necessary to sustain the wave packet against both dissipation and barotropic decay. This disturbance evolution within the wave packet differs from that in a single zonal wavenumber baroclinic life cycle, where the zonal dispersion of wave activity is absent and disturbances originate in the lower troposphere (‘‘Petterssen Type A cyclogenesis’’). However, once the disturbance reaches the packet center and the low-level disturbance has been ‘‘induced,’’ the structure of the disturbance is remarkably similar to that for a single zonal wavenumber baroclinic lifecycle.

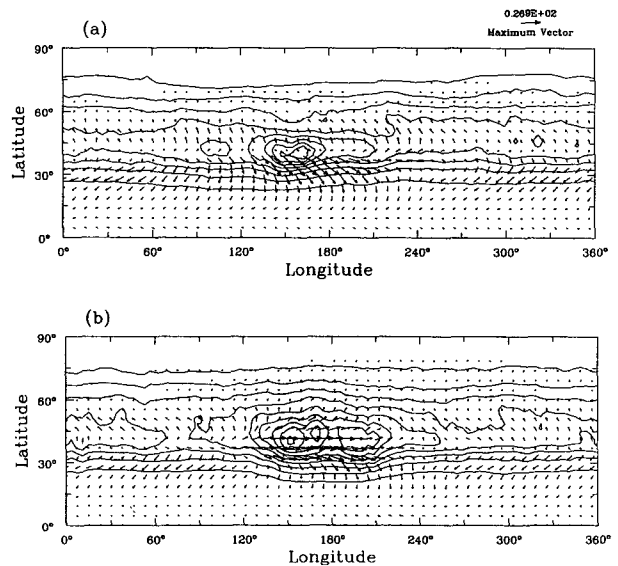


FIG. 11. Horizontal cross section of the M_R vector, defined by (5), at 350 mb for the (a) positive and (b) negative phases of $e_1(n)$. The contours are the vertical component of the M_R vector at 830 mb. The contour interval is $0.05 \text{ m}^2 \text{ s}^{-2}$.

6. PZ-averaged zonal wind EOFs

As stated in section 4, the EOFs of the PZ-averaged zonal wind were not quite as useful as $e_1(n)$. However, the structures of the first two EOFs of the PZ-averaged zonal wind, referred to as $e_1(U)$ and $e_2(U)$, are worth examining. The structures of $e_1(U)$ and $e_2(U)$ are shown in Figs. 12b and 12c, respectively. The variance of the first and the second EOF is 17.9% and 14.5%, respectively. We also found that these two EOFs are distinct. By adding these EOFs to the climatological PZ-averaged zonal wind (Fig. 12a), we notice that $e_1(U)$ represents both modulation of the jet strength in the upper troposphere and meridional displacement of the jet in the lower troposphere. On the other hand, $e_2(U)$ represents both modulation of the jet strength in the lower troposphere and meridional displacement of jet in the upper troposphere.

We point out that the difference in the PZ-averaged zonal wind composite (Fig. 5j) of $e_1(n)$ shows remarkable similarity with $e_2(U)$ (Fig. 12c), in particular equatorward of 45° latitude. In fact, the linear correlation between the principal components of $e_1(n)$ and $e_2(U)$ is 0.63, which is statistically significant above the 99% confidence level. Not surprisingly, the composite EP fluxes for $e_2(U)$ (not shown) somewhat resemble the EP fluxes shown in Figs. 5a and 5b, respectively. However, the difference is much less distinctive than that between Figs. 5a and 5b. We also examined the composite EP fluxes for the first, third, and fourth EOFs, but none of them showed characteristics of the AB or CB cases for either phase of the EOFs. Because $U - ca \cos \phi$ is the denominator of the first term in (2), one expects that relatively small differences in the zonal wind can result in relatively large differences in the refractive index near the critical latitudes. It is tempting to believe that this is the main reason why the PZ-averaged QG refractive index can better characterize the AB and CB than the PZ-averaged zonal wind, despite the similarity between Figs. 12c and 5j.

7. Concluding remarks

In an aquaplanet GCM, the two distinct types of wave breaking described in THM are shown to exist. The QG refractive index obtained in the "center wave" is shown to be useful for distinguishing the two types of wave breaking. We use the composite EP flux and its divergence for either phase of the first EOF of the refractive index, $e_1(n)$, to show that the positive (negative) phase of $e_1(n)$ corresponds to the AB (CB) case. The central characteristic of the positive phase is wave breaking of a thinning trough on the equatorward side of the jet, while that of the negative case is vortex roll-up followed by decay on the poleward side of the jet; although the negative phase shares many similar characteristics with those of the LC2 case in THM, we do

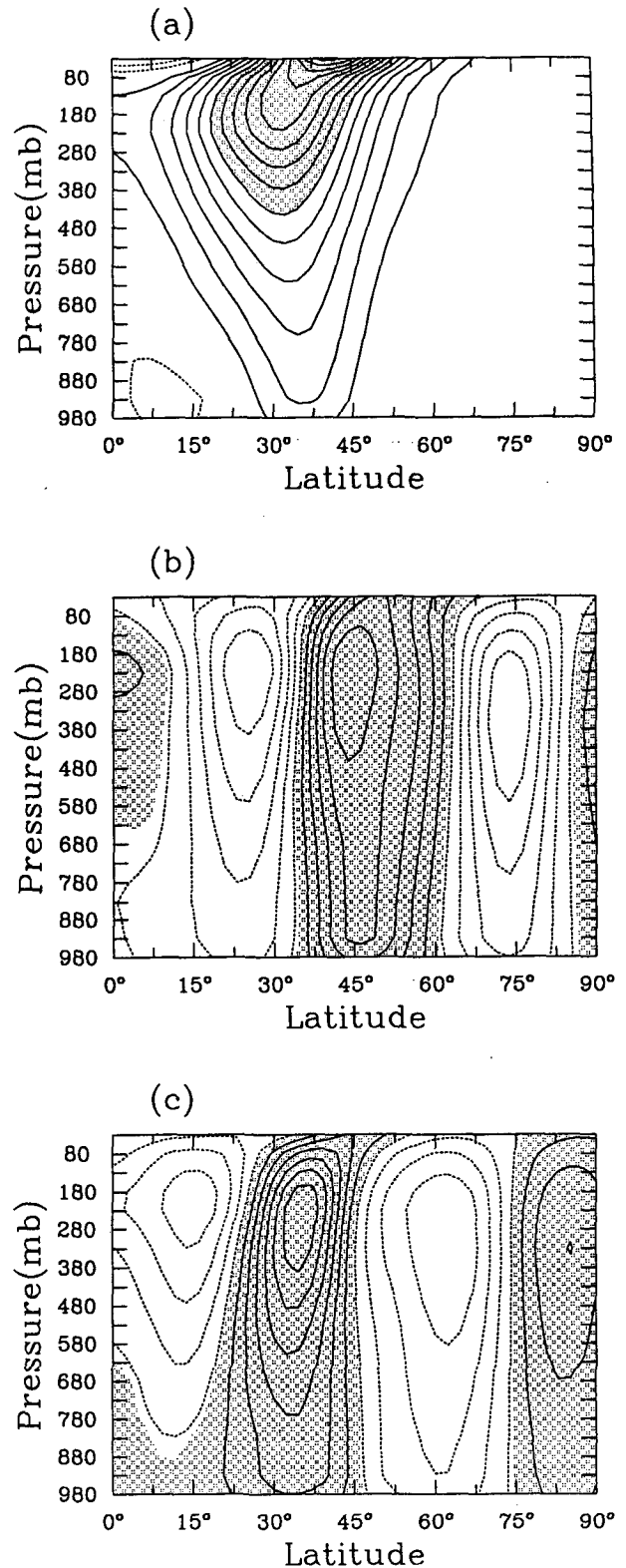


FIG. 12. Meridional cross section of the (a) time-mean PZ-averaged zonal wind, (b) first EOF, and (c) second EOF of the PZ-averaged zonal wind. The contour interval for (a) is 5 m s^{-1} , and the region where $U > 30 \text{ m s}^{-1}$ is shaded. The contour intervals for (b) and (c) are arbitrary.

not find undulation as described in THM. This morphology is shown both for a few snapshots and for composites of potential temperature on the nominal tropopause surface. We also note that the EKE of the positive case is smaller than that of the negative case, even though the baroclinicity of the basic state is greater for the positive case; the value of the baroclinicity parameter averaged over 30° and 45° latitude, using the Eady growth rate as in Hoskins and Valdes (1990), is 0.49 day⁻¹ and 0.40 day⁻¹ for the positive and negative cases, respectively.

It is also important to mention that even though two distinct types of wave breaking have been found, these results do not imply bimodality. A histogram of the principal component of $e_1(n)$ showed that the relative frequency (number of observations) varies smoothly between extreme positive and negative values, with greatest frequency occurring at a positive value for the principal component. Because the variance of $e_1(n)$ is small, it is difficult to make any general statement about the type of wave breaking, but the above analysis leads us to interpret AB and CB as two extreme types of wave breaking; more often, however, the nonlinear waves show intermediate features, with characteristics tending more toward AB. This preference for AB is consistent with numerous observational and theoretical studies.

We also examined the composite EP flux and its divergence based on the principal components of the EOFs of other quantities, such as PZ-averaged zonal wind, meridional shear of the PZ-averaged zonal wind, and vertically averaged meridional shear of the PZ-averaged zonal wind (the latter two composites were not discussed in the main body of this paper). We found that none of these shows as distinctive EP cross sections as those based on $e_1(n)$. However, for the reasons stated in section 4, we do not claim that the QG refractive index is the best quantity for objective distinction between AB and CB. As our understanding of nonlinear dynamics improves, a better quantity might emerge.

Because there is no obvious external forcing in the aqua-planet GCM, such as stationary waves to drive the basic flow toward being more suitable for either type of wave breaking, we believe that their variability is eddy driven. One possible scenario is that as the waves break and are absorbed at their critical latitudes in the subtropics, as in the AB case, the potential vorticity in the critical layer will be homogenized, resulting in a less absorbing critical layer (Killworth and McIntyre 1985). As the property of the critical layer changes, so does the behavior of the baroclinic waves; instead CB takes place. However, radiative relaxation will eventually restore the meridional potential vorticity gradient, recovering the critical layer as a strong absorber once again. If this picture is correct, we suspect that the frequency distribution of the AB and CB states will crucially depend on the radiative relaxation

timescale. We also believe that this variability can be valuable information for understanding some of the observed low-frequency variability. In order to test this hypothesis, it will be useful to perform forced-dissipative lifecycle calculations (Barnes and Young 1992) with varying radiative relaxation timescales.

The composite PZ-averaged zonal wind difference between the positive and negative cases possesses an essentially equivalent barotropic structure with largest amplitude in the upper troposphere, indicating that the meridional shear of the zonal wind in the upper troposphere, rather than the barotropic shear as in THM, is a crucial factor that determines the characteristics of the baroclinic wave breaking. Perhaps this is to be expected because the wave activity propagates into the upper troposphere as the waves grow.

The distinctly different nonlinear evolution of the baroclinic waves can also be important for understanding variability of storm tracks; along the jet core, both the composite PZ-averaged zonal wind and the baroclinicity parameters measured either by the Eady growth rate or by the vertical shear between 250 and 750 mb are greater for the positive case than for the negative case, yet the EKE for the positive case is smaller than that for the negative case. These zonal wind and EKE characteristics for the positive case, relative to those of the negative case, are quite similar to those for the midwinter Pacific jet. Nakamura (1992) found that the strength of the Northern Hemisphere (NH) storm track exhibited a minimum in the midwinter when the baroclinicity is at its maximum. This behavior is more pronounced in the Pacific than in the Atlantic storm track. There are several potential explanations for this seemingly counterintuitive behavior. One possibility is that linearly unstable mode in the Pacific region becomes convectively, rather than absolutely, unstable during midwinter because of the increased vertically averaged wind in that region (Pierrehumbert 1984). However, the smaller EKE for the positive case with its strong PZ-averaged zonal winds suggests that the nonlinear equilibrium process of baroclinic waves may also be able to account for the midwinter minimum in the NH storm track. It may well be possible that as the Pacific jet becomes stronger and sharper in midwinter, baroclinic waves have a greater tendency to behave as in the positive (i.e., AB) case, resulting in smaller EKE, or weaker storm activity.

The three-dimensional structure of the horizontal winds and potential temperature, or potential vorticity, suggest that the upper-level PV may induce the lower-level PV downstream of the packet center, but such a link is much weaker upstream of the packet center. Consistent with this speculation, the zonal cross section of the wave activity vector, \mathbf{M}_R (Plumb 1986), shows that the wave activity propagates eastward relative to the time-mean flow, that is, downstream development, and is confined to the upper troposphere; in the lower troposphere, the vertical component of \mathbf{M}_R , represent-

ing the heat flux, dominates. However, the value of the zonal component of M_R remains essentially the same at either boundary of the center wave, allowing the use of diagnostics for waves on a zonally symmetric flow.

Acknowledgments. We would like to thank Drs. Jeffrey Whitaker, Albert Barcilon, and Prashant Sardeshmukh and two anonymous reviewers for their beneficial comments on this manuscript. We also thank Peter Philippis of GFDL for performing the integration of the aqua planet GCM. This work was supported by the NOAA Climate and Global Change Program.

APPENDIX

Complex Demodulation

Demodulation is a process that separates the modulating packet from the carrier wave. Consider a set of data containing a perturbation of the form

$$\psi(x) = \text{Re}[A \exp\{i(k_0x + \varphi)\}], \quad (\text{A1})$$

where A and φ are slowly changing amplitude and phase, respectively. Given the value of k_0 , that is, the carrier wavenumber, we define a new function,

$$\tilde{\psi}(x) = \psi(x) \exp(-ik_0x). \quad (\text{A2})$$

By substituting (A2) into (A1), we obtain

$$\tilde{\psi}(x) = \frac{1}{2} A \exp(i\varphi) + \frac{1}{2} A \exp\{-i(2k_0x + \varphi)\}. \quad (\text{A3})$$

In general, the data do not consist of purely sinusoidal disturbances. Therefore, we also need to consider a noise component. The aim of complex demodulation is to separate the first term in (A3) from the second and from the noise, assuming that 1) both A and φ are smooth, and therefore the first term is smooth as well, and that 2) the noise has no component at wavenumber k_0 . Under these assumptions, the smooth component of $\tilde{\psi}(x)$ can be obtained by linear filtering.

Therefore, given a meridional wind field (or eddy streamfunction field) at a fixed latitude and time, we first carry out spectral analysis to find the most dominant zonal wavenumber and regard it as the carrier wavenumber k_0 . Then we multiply the meridional wind field by $\exp(-ik_0x)$, following (A2). Next, in order to remove the second term in (A3), we apply a linear smoothing filter to (A3). Finally, we obtain the slowly varying amplitude by taking the absolute value of the smoothed $\tilde{\psi}(x)$ multiplied by two. We found that the resulting envelope or packet structure is insensitive to the slight variation in k_0 . For example, suppose that the most dominant zonal wavenumber is 6, and the second dominant wavenumber is 5. The result is essentially unchanged whether k_0 is fixed at 6 or at 5. This pro-

cedure is repeated for each latitude and model day; for a given day, we average the envelope function over a 10° latitude band centered around the midlatitude jet maximum.

REFERENCES

- Andrews, D. G., and M. E. McIntyre, 1976: Planetary waves in horizontal and vertical shear, the generalized Eliassen–Palm relation and the mean zonal acceleration. *J. Atmos. Sci.*, **33**, 2031–2048.
- Barnes, J. R., and R. E. Young, 1992: Nonlinear baroclinic instability on the sphere: Multiple life cycles with surface drag and thermal damping. *J. Atmos. Sci.*, **49**, 861–878.
- Blackmon, M. L., J. M. Wallace, N.-C. Lau, and S. L. Mullen, 1977: An observational study of the Northern Hemisphere. *J. Atmos. Sci.*, **34**, 1040–1053.
- Chang, K. M., 1993: Downstream development of baroclinic waves as inferred from regression analysis. *J. Atmos. Sci.*, **50**, 2038–2053.
- Charney, J. G., 1947: The dynamics of long waves in a baroclinic westerly current. *J. Meteor.*, **4**, 135–163.
- Eady, E. T., 1949: Long waves and cyclone waves. *Tellus*, **1**, 33–52.
- Edmon, H. J., Jr., B. J. Hoskins, and M. E. McIntyre, 1980: Eliassen–Palm cross sections for the troposphere. *J. Atmos. Sci.*, **37**, 2600–2616.
- Feldstein, S. B., 1994: A weakly nonlinear primitive equation baroclinic lifecycle. *J. Atmos. Sci.*, **51**, 23–34.
- , and I. M. Held, 1989: Barotropic decay of baroclinic waves in a two-layer beta-plane model. *J. Atmos. Sci.*, **46**, 3416–3430.
- , and S. Lee, 1995: The intraseasonal evolution of angular momentum in aqua-planet and realistic GCMs. *J. Atmos. Sci.*, **52**, 625–649.
- Hoskins, B. J., and P. Barrisford, 1988: The storm of 15–16 October 1987: A potential vorticity perspective. *Wea.*, **43**, 122–129.
- , and P. J. Valdes, 1990: On the existence of stormtracks. *J. Atmos. Sci.*, **47**, 1854–1864.
- , M. E. McIntyre, and A. W. Robertson, 1985: On the use and significance of isentropic potential vorticity maps. *Quart. J. Roy. Meteor. Soc.*, **111**, 877–946.
- Karoly, D. J., and B. J. Hoskins, 1982: Three dimensional propagation of planetary waves. *J. Meteor. Soc. Japan*, **60**, 109–123.
- Killworth, P. D., and M. E. McIntyre, 1985: Do Rossby-wave critical layers absorb, reflect or over-reflect? *J. Fluid Mech.*, **161**, 449–492.
- Lee, S., and I. M. Held, 1993: Baroclinic wave packets in models and observations. *J. Atmos. Sci.*, **50**, 1413–1428.
- Lindzen, R. S. 1988: Instability of plane parallel shear flow (toward a mechanistic picture of how it works). *Pure Appl. Geophys.*, **126**, 103–121.
- Matsuno, T., 1970: Vertical propagation of stationary planetary waves in the winter Northern Hemisphere. *J. Atmos. Sci.*, **27**, 871–883.
- Nakamura, H., 1992: Midwinter suppression of baroclinic wave activity in the Pacific. *J. Atmos. Sci.*, **49**, 1629–1642.
- Nakamura, M., and R. A. Plumb, 1994: The effects of flow asymmetry on the direction of Rossby wave breaking. *J. Atmos. Sci.*, **51**, 2031–2045.
- Nigam, S., and R. S. Lindzen, 1989: The sensitivity of stationary waves to variations in the basic state zonal flow. *J. Atmos. Sci.*, **46**, 1746–1768.
- North, G. R., T. Bell, F. Modeng, and R. F. Cahalan, 1982: Sampling errors in the estimation of empirical orthogonal functions. *Mon. Wea. Rev.*, **110**, 699–706.
- Orlanski, I., and K. M. Chang, 1993: Ageostrophic geopotential fluxes in downstream and upstream development of baroclinic waves. *J. Atmos. Sci.*, **50**, 212–225.
- Palmer, T. N., 1982: Properties of the Eliassen–Palm flux for planetary-scale motions. *J. Atmos. Sci.*, **39**, 992–997.
- Petterssen, S., 1956: *Weather Analysis and Forecasting*. Vol. I. McGraw-Hill, 428 pp.

- Pierrehumbert, R. T., 1984: Local and global baroclinic instability of zonally varying flow. *J. Atmos. Sci.*, **41**, 2141–2162.
- Plumb, R. A., 1986: Three-dimensional propagation of transient quasigeostrophic eddies and its relationship with the eddy forcing of the time-mean flow. *J. Atmos. Sci.*, **43**, 1657–1678.
- Randel, W. J., and J. L. Stanford, 1985: The observed lifecycle of a baroclinic instability. *J. Atmos. Sci.*, **42**, 1364–1373.
- Simmons, A. J., and B. J. Hoskins, 1978: The lifecycles of some nonlinear baroclinic waves. *J. Atmos. Sci.*, **35**, 414–432.
- , and ———, 1980: Barotropic influences on the growth and decay of nonlinear baroclinic waves. *J. Atmos. Sci.*, **37**, 1679–1684.
- Thorncroft, C. D., B. J. Hoskins, and M. E. McIntyre, 1993: Two paradigms of baroclinic-wave life-cycle behavior. *Quart. J. Roy. Meteor. Soc.*, **119**, 17–55.
- Whitaker, J. S., and C. Snyder, 1993: The effects of spherical geometry on the evolution of baroclinic waves. *J. Atmos. Sci.*, **50**, 597–612.